Australasian Physical & Engineering Sciences in Medicine (2019) 42:745–756
https://doi.org/10.1007/s13246-019-00774-1

SCIENTIFIC PAPER

Dose perturbation by metallic biliary stent in external beam radiotherapy of pancreato-biliary cancers

Ho Lee[1] · Jeongmin Yoon[2] · Kwangwoo Park[2] · Chai Hong Rim[2] · Moon Jae Chung[3] · Jinsil Seong[2]

Received: 11 January 2019 / Accepted: 29 June 2019 / Published online: 8 July 2019

Abstract

This study aims to investigate dose perturbations caused by a metallic biliary stent (MBS) in patients undergoing external beam radiotherapy for cancers in the pancreato-biliary region. Four MBSs with nitinol mesh were examined in the EasyCube® phantom including a custom stent holder fabricated by a 3D printer. For experimental models, three-dimensional conformal radiotherapy plans using a single anterior–posterior (AP) and four-field box (4FB) as well as volumetric modulated arc therapy (VMAT) plan were prepared to deliver the photon beam of 8 Gy to the stent holder. EBT3 film was used to measure dose distributions at four sides surrounding MBS. All MBSs in the AP beam demonstrated mean dose enhancements of 2.3–8.2% at the proximal, left, and right sides. Maximum dose enhancements of 12.3–19.5% appeared at regions surrounding the radiopaque markers. At the location distal to the source, there were mean dose reductions of − 3.6 to − 10.9% and minimum doses of − 11.1 to − 9.5%. The mean and maximum doses with the 4FB plan were in the ranges of − 0.1 to 3.6% and 6.7–14.9%, respectively. The VMAT produced mean doses of − 0.9 to 4.8% and maximum doses of 6.0–15.3%. Dose perturbations were observed with maximum and minimum spots near the stent surface. The use of multiple beams including parallel-opposed pairs reduced dose perturbations caused by the nitinol and radiopaque components within the stent. Special attention is required for patients in whom the radiopaque markers are closely located near critical structures or the target volume.

Keywords Metallic biliary stent · Dose perturbation · 3D printer · External beam radiation · Cancers in the pancreato-biliary region

Introduction

Cancers in the pancreato-biliary region (CPB) are one of the most challenging malignancies for oncologists. Surgical resection is the only potentially curative treatment; however, chemoradiotherapy is often considered because most patients present with unresectable disease at the time of diagnosis [1–5]. CPB are frequently accompanied by biliary obstruction, which could be resolved with metallic biliary stents (MBS). MBS has a substantial amount of metal as its component, which can cause perturbation of dose distribution on radiation. This phenomenon has well been documented in the patients with self-expandable stent within esophagus, showing dose perturbations either in increase or in decrease of radiation doses at the interface of the stent and surrounding tissues [6–11]. In the case of CBP, there have been very few studies on the radiation dose perturbation by MBS distribution. Considering that adjacent organs to CPB are radiosensitive in nature, unexpected change in radiation dose distribution might result in serious toxicity involving ulcers, hemorrhage, obstruction, stricture, and even perforation [12, 13]. In this study, we examined whether dose perturbation presented using MBS at current clinical use. We also investigated quantification of dose perturbation using three-dimensional conformal radiotherapy (3D-CRT) and volumetric modulated arc therapy (VMAT) techniques [14].

✉ Jinsil Seong
JSSEONG@yuhs.ac

[1] Department of Radiation Oncology, Gangnam Severance Hospital, Yonsei University College of Medicine, 211 Eonju-ro, Gangnam-gu, Seoul 06273, Republic of Korea

[2] Department of Radiation Oncology, Yonsei Cancer Center, Yonsei University College of Medicine, 50 Yonsei-ro, Seodaemun-gu, Seoul 03722, Republic of Korea

[3] Division of Gastroenterology, Department of Internal Medicine, Yonsei University College of Medicine, 50 Yonsei-ro, Seodaemun-gu, Seoul 03722, Republic of Korea

Materials and methods

Metallic biliary stents

Of the available covered or uncovered MBSs [15], four clinically available MBSs with nitinol mesh were considered in our study: silicon covered stent (MiTech Ltd. Republic of Korea), single bare stent, double bare stent, and large open cell stent (all three from Taewoong Ltd, Republic of Korea). The four MBSs have self-expandable structures, which expand and commonly reach it nominal length and diameter because nitinol is a metal alloy of nickel and titanium having a memory-effect [16]. These self-expandable MBSs are generally provided in a constraining sheath attached to a delivery catheter that accepts a guide wire. After removal of the constraining sheath, they are cylindrical in shape with an outer diameter of 10 mm and a nominal length of 80 mm (Fig. 1). A small number of radiopaque markers such as gold (atomic number of $Z = 79$ and a mass density of 19.3 g/cm^3) or platinum ($Z = 78$ and 21.45 g/cm^3) are included on the stent mesh for localization purposes. Each localization marker is approximately 2–3 mm in diameter. The silicon covered stent contains 12 gold radiopaque markers attached to four on both ends of the stent and four at the center. The single bare and large open cell stents have eight platinum radiopaque markers, three on both ends and two at the center. The double bare stent comprises 24 platinum radiopaque markers, 10 on both ends and four at the center.

Fabrication of a custom stent holder

Figure 2 illustrates the schematic design and custom stent holder fabricated by the 3D printer. As shown in Fig. 2a and b, a virtual 3D-printable stent holder was sectioned in the upper and lower parts for ease of reproducible placement of the biliary stent and pieces of film. Each part with a sliding slot was designed by OpenSCAD, which is free for use in any institution and makes it possible to save the stereolithography (STL) file format that can be read by 3D printer applications. The virtual stent holder is a rectangular parallelepiped of $10 \times 2 \times 2$ cm^3 and contains an air-filled cylinder-like cavity to place a biliary stent. The empty space is 10 mm in diameter and 80 mm long to accommodate a long, narrow MBS that shortens to the nominal length of a MBS in the body during deployment [16]. This is based on the fact that the air cavity is clearly shown inside the stent in a planned CT acquired from an actual patient. As shown in Fig. 2c, two hollows of $63.7 \times 16.7 \times 0.6$ mm^3 were created on the sliding slot for pieces of film placed at two locations proximal and distal to the radiation source. Four recesses of $63.7 \times 5.6 \times 0.6$ mm^3 were made in both upper and lower parts so that two

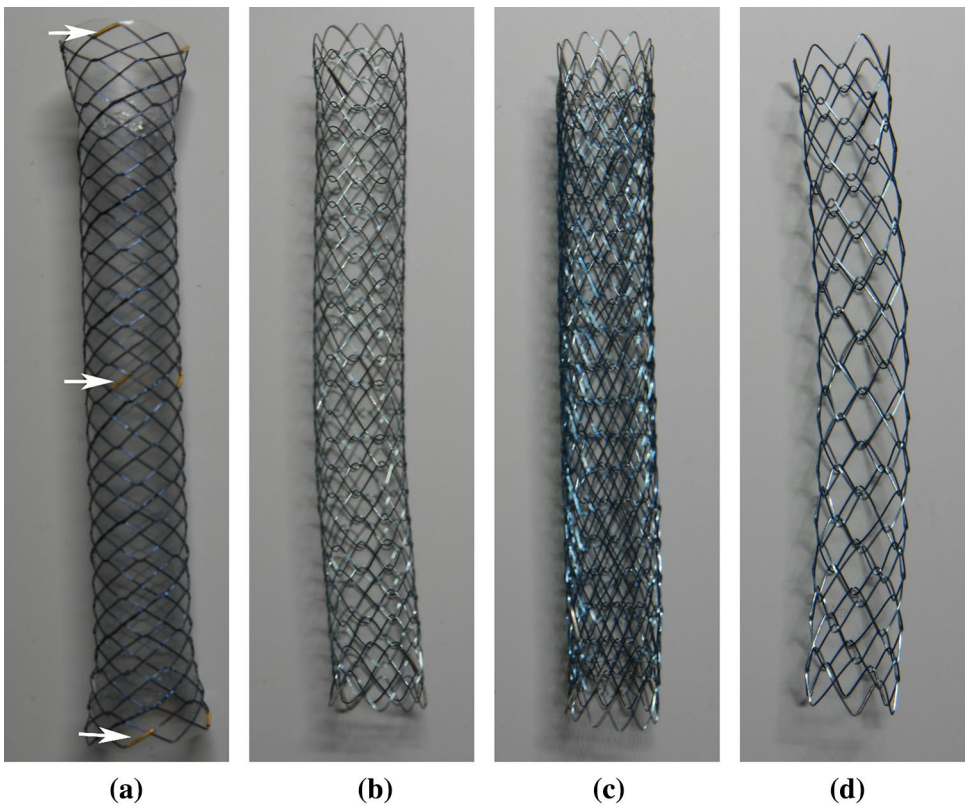

Fig. 1 Clinically available MBSs with different mesh types: **a** silicon covered stent, **b** single bare stent, **c** double bare stent, and **d** large open cell stent. Arrows denote radiopaque markers

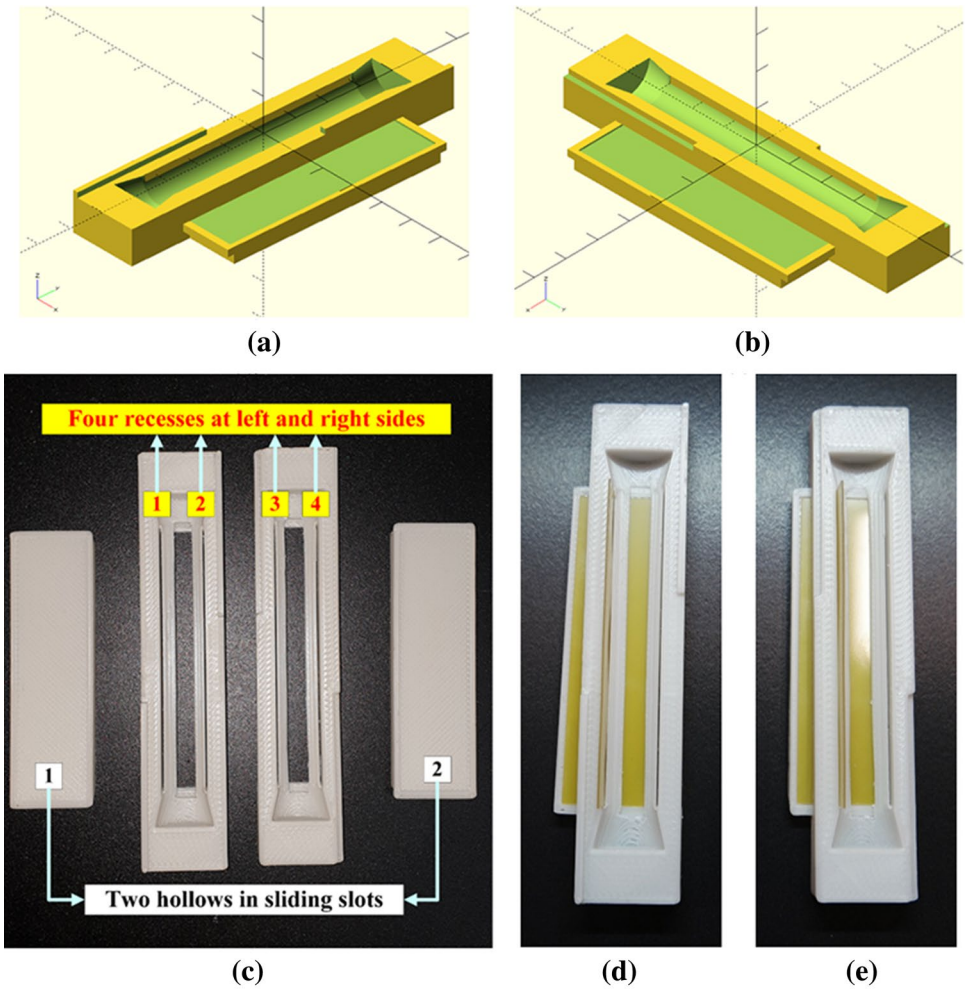

Fig. 2 The upper part with a sliding slot and the lower part with a sliding slot of a custom stent holder: **a**, **b** virtual biliary stent holders designed by OpenSCAD, **c** four parts of the custom stent holder fabricated by a 3D printer, and **d**, **e** the upper and lower parts including four pieces of film

pieces of film are placed on the left and right sides near the biliary stent. After finishing the design, the printing software KISSlicer was used, which is available under an open-source license. The printing parameters were speed of 30 mm/s, layer thickness of 2.5 mm, and infill ratio of 100%. The other parameters were determined after the calibration process. Based on these parameters, the holder was fabricated with a 3D printer (CubeX; 3D Systems Ltd., USA), using a polylactic acid (PLA) filament with a physical density (ρ) of 1.25 g/cm^3. According to recent studies [17, 18], the actual 3D printed density is different from the preset infill density. For precise dosimetric studies, a CT scan with the 3D printed stent holder was performed to calculate the actual density by comparing the image value-to-density table. The actual density of the 3D printed stent holder is 1.145 g/cm^3. The upper and lower sections of the custom stent holder that includes two sliding slots and four pieces of film are shown in Fig. 2d and e.

Measurements and data analysis

All measurements were performed in the oval EasyCube® phantom (Sun Nuclear Corporation, FL, USA) with the custom stent holder to facilitate reproducible positioning and irradiation conditions for four biliary stents (Fig. 3). The EasyCube® phantom consists of water equivalent material with a physical density of 1.045 g/cm^3 and is commonly used as a delivery quality assurance (DQA) tool for pretreatment dosimetric evaluations. Dose distributions were measured with GAFCHROMIC EBT3 film (Ashland Specialty Ingredients, NJ, USA) due to its high spatial resolution. Using a laser cutting system, the film was cut to several pieces of two different sizes: 63.7×16.7 mm^2 and 63.7×11.2 mm^2. The custom stent holder allowed pieces of film to be placed at four locations, proximal, distal, left, and right, to the radiation source for each stent as shown in Fig. 3a. Two pieces of film sized 63.7×16.7 mm^2 were placed into a sliding slot directly above (proximal to the radiation source) and

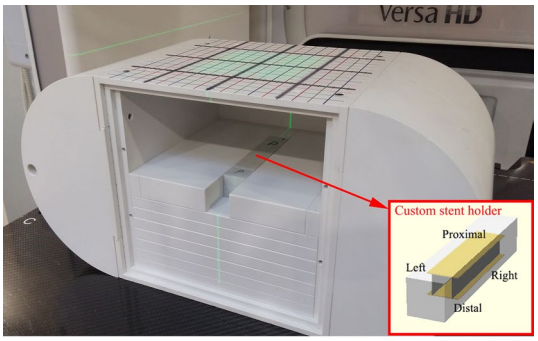

(a)

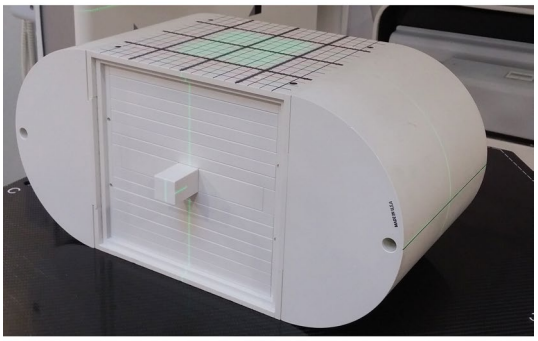

(b)

Fig. 3 The EasyCube® phantom setup with a custom biliary stent holder: **a** position of the custom stent holder illustrating its internal structure and **b** external structure

below (distal to the radiation source) each stent, on planes orthogonal to the radiation beam. The other two pieces of film sized 63.7×11.2 mm^2 were inserted in two recesses on the left and right sides of the stent holder parallel to the radiation beam. The central region of each piece of film was in direct contact with the stent.

The custom stent holder was positioned at the center of the EasyCube® phantom such that the central axis of the beam was perpendicular to the cylindrical axis of the biliary stent, which was positioned at the mechanical isocenter, i.e., usually at 100 cm source-to-axis distance (SAD). This isocentric setup allows the best isodose distribution in terms of dose uniformity, making it easy to understand the forward and back scatter dose perturbations caused from a stent. Care was taken during the EasyCube® setup and positioning of the biliary stent replacement. The EasyCube® phantom surface markers were aligned with respect to the room lasers prior to each stent measurement. For experimental models, two 3D-CRT and one VMAT plans were prepared to deliver the photon beam of 8 Gy dose with energy of 6MV incident to the center of the phantom using the Monaco® 5.11 (Elekta AB, Stockholm, Sweden) treatment planning system (TPS). The Monte Carlo (MC) dose calculation algorithm [19] was applied with the settings of the grid spacing of 2 mm and the statistical uncertainty of 0.5% per control point. For 3D-CRT plans, the single anterior–posterior (AP) technique and four-field box (4FB) technique [20] were used with a field size of 10×10 cm^2 and 100 cm SAD. To examine the possibility that the hot spot created by one beam is cancelled by a cold spot generated by the opposing beam, we created an 4FB plan where opposite beams were added and the cylindrical axis of the stent is at the same depth for each beam. For practical evaluation for clinical use, a DQA plan based on the patient plan with VMAT was created using a single arc surrounding the center of the phantom. Based on these plans, beam delivery was performed using a Versa HD™ linear accelerator system (Elekta Limited, Stockholm, Sweden) to each of the four MBSs and a control setup. For the control setup, only the custom stent holder, without a stent, was placed in the same position. The EasyCube® phantom setup illustrating its external structure is illustrated in Fig. 3b. All measurements were performed twice to verify the reproducibility of the results. An experienced radiation physicist performed all measurements.

All films were processed to quantify the dose perturbations next to the stents at locations proximal, distal, left, and right to the radiation source. The piece of film proximal to the radiation source was used to measure the backscattered radiation, the piece of film distal to the radiation source was used to measure the radiation dose perturbations caused by the absorption and scatter properties of the stent, and the pieces of film at the left and right positions were used to measure the lateral scattering. The exposed films were digitized with a commercially available Epson Expression 11000XL flatbed scanner. For each film, the 16-bit red channel was used for analysis. The results were analyzed with the RIT software package (RIT, Denver, CO, USA). Dose calibration was performed with GAFCHROMIC EBT3 film on the same linear accelerator system, using a conventional technique [21] with exposures over the range 0 to 15 Gy. Each film piece was placed at a 5 cm depth with a 10 cm × 10 cm field size and a 100 cm SAD in a water-equivalent RW3 phantom (PTW Freiburg, Freiburg, Germany), which consisted of 30 cm × 30 cm slabs of different thicknesses and a housing plate for ionization chamber. The total thickness of the phantom was 15 cm. The monitor units in terms of absorbed doses were determined by using A1SL chamber (Standard Imaging, WI, USA) within the dose range of interest. The films were exposed to 18 absorbed doses to cover the full dynamic range of the film. The 3rd degree polynomial function was used as the film calibration curve fitter as shown in Fig. 4. The difference between the measured value and the corresponding fitted value is displayed as a residual indicating how far the corresponding point on the fitted line is from the measured data. A – 1.4% mean uncertainty level with a standard deviation of 2.9% was achieved in the dose range from 5 to 15 Gy. In particular, at an interesting dose level that delivers 8 Gy to

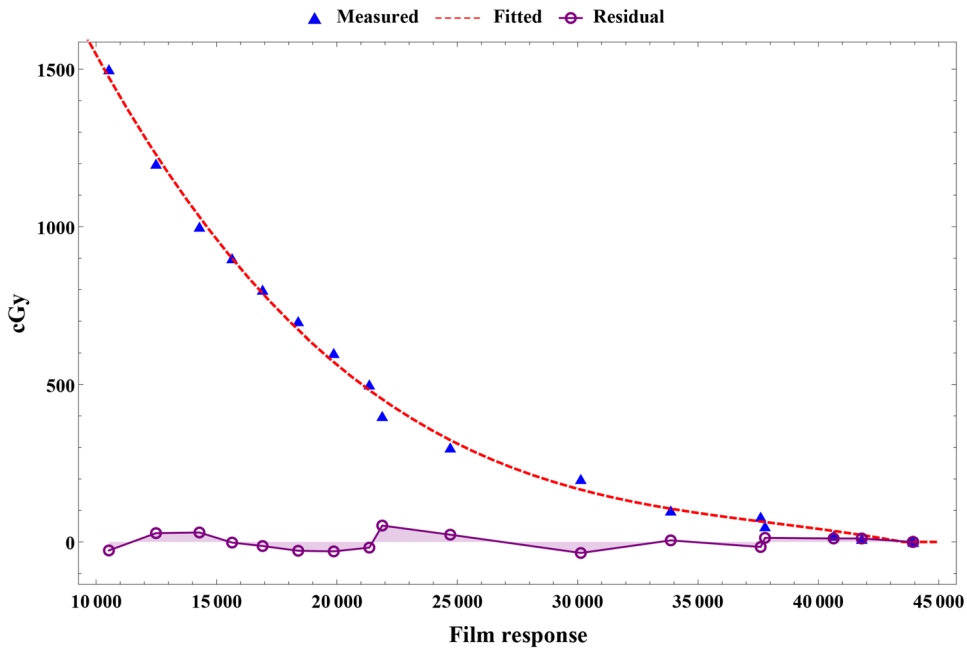

Fig. 4 Dose calibration curve representing the relationship between absorbed dose and film response in the range of 0 to 15 Gy

the planning target volume, a residual dose of − 1.6% was seen. To gain precise and reproducible results in film dosimetry, the scanning of the films with the same period (22 h irradiation-to-scanning time) after irradiation was performed on the same orientation because process consistency is crucial to reduce potential uncertainties such as dose dependent post irradiation darkening and relative deviations in portrait to landscape orientation [22].

All of the examined biliary stents were symmetric, so uniform regions of interest (ROIs) corresponding to the center of each film (54 × 5 mm^2 subsets) were chosen for analysis. In addition, 10 × 5 mm^2 subsets between the end and the center of the stent were selected to exclude the regions of film corresponding to the gold or platinum radiopaque markers from the analysis. This eliminated artifacts at the edge of each film. A 5 × 5 median filer was applied for each film subset, and random outliers were excluded from the analysis. The range of dose perturbations caused by the stents was determined by the dose histogram representing the percent differences between corresponding pixels of each stent film and the uniformly irradiated film in the control setup, measured at the proximal, distal, left, and right locations. Results were analyzed as maximum, mean, and minimum values extracted from the dose histogram.

Qualitative evaluations of the four MBSs were performed to visually compare the patterns of dose perturbations at the proximal and distal sides surrounding the stent by capturing uniform ROIs (10 × 5 mm^2 subsets) corresponding to the center of each film measured by a single AP beam, 4FB beam, and VMAT delivery. To analyze how the distinct patterns such as hot and cold spots appear at four sides surrounding MBS, we also compared a degree of overlap between dose histograms obtained with 10 × 5 mm^2 subsets of each film.

Results

The degree of radiation dose perturbations quantified for the four MBSs by varying the design of the stent mesh is presented in Table 1. The average of the two measurements was reported as a representative estimate and its uncertainty estimate was based on the absolute value of the difference between each measurement and the average value. All MBSs demonstrated mean dose enhancements of 2.3–8.2% from a single AP beam at locations proximal, left, and right to the radiation source due to back- or side-scattered radiation. At the regions of film surrounding the radiopaque markers attached to assist during fluoroscopically guided placement, there were larger maximum doses and dose perturbations, with the maximum increases (up to 19.5%) in dose distribution generated by the double bare stent. Additionally, all four MBSs created increased and decreased dose distributions at the location distal to the radiation source due to the scatter and attenuation properties of the stents. Mean dose reduction was in the range of − 3.6% to − 0.9%, and minimum doses ranging from − 11.1 to − 9.5% occurred at the locations of the radiopaque markers. A slightly lower achieved dose was expected in the double bare stent because it is shadowed more by the stent in stent during a single AP beam. In the 4FB, reduced dose perturbations ranging from − 0.1 to 3.6% were seen on all stent walls as compared to the single AP beam. Maximum dose enhancements of 6.7% to 14.9% occurred near the radiopaque localization markers. Mean

Table 1 Dose perturbation ranges of four MBSs measured from regions of interest (ROIs) corresponding to the center of each film (54×5 mm^2 subsets) at locations proximal, distal, left, and right to the radiation source using single AP, 4FB, and single arc VMAT techniques

	Proximal		Distal		Left		Right	
	%	cGy	%	cGy	%	cGy	%	cGy
Single AP technique								
Silicone covered								
Min	−3.1±0.3	−27.9±3.4	−10.9±0.6	−89.7±7.7	−2.3±0.1	−19.8±0.4	−3.8±0.0	−31.9±0.2
Mean	4.9±0.3	40.7±1.3	−0.9±0.1	−7.4±0.8	5.7±0.3	45.5±3.2	3.0±0.4	24.2±3.6
Max	17.9±0.8	142.4±1.8	6.9±0.2	54.7±2.6	16.4±0.3	130.1±4.7	13.7±0.1	106.2±1.6
Single bare								
Min	−3.9±0.1	−33.8±0.3	−9.5±0.2	−78.0±3.8	−3.0±0.1	−24.8±0.8	−5.3±0.8	−44.7±6.4
Mean	5.1±0.4	42.3±1.8	−2.1±0.1	−17.6±0.2	4.9±0.3	38.9±3.7	2.3±0.6	18.6±5.1
Max	15.2±0.5	124.3±1.7	5.4±0.4	43.1±3.7	13.1±0.5	105.1±5.0	12.3±0.4	95.2±5.4
Double bare								
Min	−0.5±0.3	−4.6±2.9	−10.9±1.3	−89.0±14.5	−1.6±0.6	−13.4±5.6	−3.4±0.2	−28.8±1.8
Mean	8.2±0.2	67.7±0.1	−3.6±0.4	−29.5±4.1	6.0±0.1	48.0±0.6	4.7±0.1	37.5±1.9
Max	19.5±0.8	155.5±10.1	5.5±0.9	44.5±7.2	14.0±0.3	107.5±5.4	13.5±0.5	104.9±6.3
Large open cell								
Min	−3.4±0.9	−30.6±8.1	−11.1±0.7	−90.4±8.3	−3.5±0.3	−29.3±1.6	−4.3±0.4	−34.2±2.1
Mean	5.0±0.9	40.8±6.2	−1.5±0.4	−12.8±3.6	4.3±0.1	34.5±0.8	3.6±0.2	29.0±2.5
Max	15.1±1.8	117.0±9.6	7.7±0.8	60.4±4.7	12.3±0.4	97.4±6.1	12.8±0.6	99.9±6.3
4FB technique								
Silicone covered								
Min	−5.5±0.8	−46.4±6.4	−6.3±1.5	−53.1±12.3	−5.3±0.6	−43.9±4.5	−3.7±0.9	−30.9±7.2
Mean	0.6±1.2	5.2±9.7	0.8±1.7	6.5±13.8	1.0±1.6	7.9±13.2	2.7±1.3	21.4±10.1
Max	7.6±1.6	60.0±12.9	8.1±2.1	60.8±18.5	12.8±1.0	95.5±8.9	11.0±2.3	84.6±18.4
Single bare								
Min	−4.4±0.5	−36.0±3.4	−4.8±0.8	−40.0±5.8	−4.0±0.1	−32.8±0.1	−3.6±1.1	−30.3±8.6
Mean	1.7±1.2	14.0±9.8	0.9±1.5	7.6±11.6	2.4±1.1	19.2±9.3	3.1±1.4	24.9±11.4
Max	7.5±2.1	58.9±16.7	8.2±1.8	62.4±14.3	12.6±0.8	94.3±6.2	9.9±2.0	75.0±16.4
Double bare								
Min	−5.6±0.2	−45.1±1.1	−9.2±1.3	−76.3±10.3	−2.7±0.1	−22.7±0.8	−4.0±0.5	−33.1±4.1
Mean	2.4±0.5	19.2±4.4	−0.1±1.0	−1.5±8.1	3.6±0.9	28.6±7.6	2.7±1.1	21.5±8.5
Max	9.5±1.2	74.4±9.2	6.7±1.8	53.6±13.1	14.9±1.7	111.1±13.4	9.3±2.1	73.0±15.7
Large open cell								
Min	−6.5±0.2	−53.5±0.8	−5.9±0.2	−49.7±1.3	−6.0±0.1	−50.4±0.9	−4.1±0.5	−34.4±4.1
Mean	0.6±0.5	5.2±3.8	0.4±0.7	3.1±5.8	0.8±0.5	6.3±4.2	2.1±0.4	16.3±3.0
Max	7.8±0.8	59.7±7.4	7.2±1.0	55.9±8.6	10.6±0.3	80.8±1.4	9.3±0.5	69.9±5.1
Single arc VMAT								
Silicone covered								
Min	−6.8±1.3	−54.9±10.1	−8.8±0.3	−72.4±2.0	−7.3±0.8	−58.0±4.7	−7.5±0.9	−58.7±4.9
Mean	1.2±1.1	9.3±8.8	−0.9±1.1	−7.1±8.4	−0.7±1.0	−5.9±8.0	0.9±1.2	7.2±9.7
Max	10.8±2.1	84.7±18.5	6.3±1.4	45.7±12.0	7.1±1.3	55.0±9.4	9.8±1.8	75.7±14.7
Single bare								
Min	−4.8±0.6	−36.4±6.0	−6.6±0.9	−50.3±6.0	−4.8±0.6	−37.5±3.7	−5.2±0.3	−37.4±0.9
Mean	2.0±0.9	15.8±7.3	0.2±1.1	1.7±8.1	1.8±0.9	13.3±7.4	1.9±0.9	14.5±7.3
Max	9.4±2.1	73.6±18.2	7.1±2.4	49.9±21.3	8.0±1.3	58.4±8.3	9.3±1.5	71.5±12.5
Double bare								
Min	−3.1±0.7	−26.0±6.4	−6.3±0.3	−48.1±1.5	−6.0±0.1	−49.5±0.8	−4.3±0.2	−34.7±1.2
Mean	4.8±0.6	36.5±6.1	0.5±0.8	4.2±6.0	1.4±0.8	10.6±6.0	2.9±0.6	22.2±5.8
Max	15.3±0.6	117.9±7.6	7.8±1.8	54.7±14.2	9.3±1.6	64.2±8.1	9.7±1.2	76.7±10.6
Large open cell								
Min	−6.5±0.7	−46.6±1.6	−5.9±0.1	−46.4±0.6	−6.0±0.5	−46.7±7.9	−4.9±2.0	−38.7±23.2
Mean	1.5±0.5	12.0±4.2	0.8±0.7	6.0±5.3	−0.1±1.4	−1.3±10.8	1.3±1.7	10.3±13.3
Max	9.8±0.8	73.8±4.6	8.6±1.3	61.4±12.0	6.0±0.1	43.6±0.5	8.6±0.1	68.0±0.1

Table 1 (continued)

Dose difference (cGy) = (measured at each stent– measured at no stent). Percent difference (%) = (measured at each stent − measured at no stent)/measured at no stent × 100%. The uncertainty estimate associated with a measurement result was based on the average absolute deviation of the two measurements

dose perturbations at the four sides from the VMAT were in the range of − 0.9% to 4.8%. Maximum dose enhancements were as high as 15.3% with the double bare stent. Multiple fields from different gantry angles effectively alleviated hot and cold spots. Table 2 lists the range of the dose perturbation in the region where the effect of radiopaque markers is negligible. All MBSs resulted in much smaller dose perturbation ranges, mainly with smaller differences between the minimum and maximum doses. We also confirmed that adding more beams (4FB and VMAT) reduced the mean dose.

Figure 5 shows visually how the patterns of dose perturbations appear on 10×5 mm^2 subsets. In the single AP beam delivery, the films from the four individual stents produced distinct patterns of increased doses measured at the proximal side and patterns of both increased and decreased doses measured at the distal side. In particular, hot spots and cold spots occurred at the locations of the radiopaque markers. However, these hot and cold spots were lower with 4FB and VMAT. As shown in Fig. 5c and d, the double bare stent caused the highest dose enhancement at the proximal side, and the large open cell stent resulted in a less prominent effect at both proximal and distal sides. These distinct patterns are shown in Fig. 6. AP technique in all MBSs split dose histograms into two sections: decreased doses at the distal side and increased doses at the proximal, left, and right sides. In contrast, the overlap areas in 4FB and VMAT techniques were increased because the use of multiple beams including parallel-opposed pairs reduced dose perturbations caused by the nitinol and radiopaque components within the stent. In particular, the large open cell stent may be more beneficial than other stents because the degree of overlap of the dose histograms obtained from the four sides is consistent within a small range, as shown in Fig. 6d.

The percentage differences between the doses obtained from actual film measurements and calculated by the Monaco® 5.11 MC algorithm are shown in Table 3. The TPS-calculated doses for the four MBSs are the minimum, mean, and maximum value within the ROI of 54×5 mm^2 at locations proximal and distal to the radiation source. An evaluation of TPS calculations versus film measurements indicates that calculated mean doses were in the ranges of − 7.1 to 1.5% at proximal side and 1.6–5.8% at distal side for three plans. Only clinically relevant are maximum and minimum doses. The maximum dose at proximal side and the minimum dose at distal side occurred at the locations of the radiopaque markers where the TPS-calculated dose in the AP beam was underestimated by 12.8% on the proximal and overestimated by 9.6% on the distal. To distinguish the second build-up and build-down effects caused by the air cavity from these values, we also assessed how well the doses obtained from actual measurement without the stent matched those calculated by the Monaco MC algorithm. The uncertainty of the TPS calculations at the interface of the air cavity was within 0.8% for two 3D-CRT plans and 2.2% for VMAT plan, respectively. As a result, the clinically available MC algorithm employed in Monaco TPS was unable to predict the effect of electron backscattering and attenuation from high atomic number materials.

Discussion

In this study, the dosimetric effect of MBSs during external beam radiotherapy of CPB was investigated using a phantom with a 3D-printed stent holder. In the case of a single incident radiation beam, all MBSs showed dose perturbations either in increase or in decrease of radiation doses at the interface of the stent and surrounding tissues, mainly due to secondary scattered electrons and attenuation properties resulting from the stent material itself. There was a relatively large difference between the doses on the left and right of the stent. This is because the spacing between the markers attached to the center of the stent is not exactly equidistant, so that the radiopaque markers on the left and right films cannot be placed symmetrically. This dose perturbation could be mitigated by using opposite beams such as 4FB or by adding multiple fields from different gantry angles such as VMAT, leading to mean dose reduction satisfying the International Commission on Radiation Units and Measurements (ICRU) recommendations that the dosimetric uncertainty in the target volume should be less than ± 5% [23]. However, considering that a radiopaque localization marker on the stent mesh can be closely abutted to the target volume, a non-negligible increase of radiation dose might result in a serious complication in radiosensitive organs adjacent to CPB.

Generally, we can expect the second build-up and build-down effects resulting from the cavity that holds MBSs. To distinguish the dose perturbations caused by the stent and the air cavity, we analyzed the percent differences between corresponding pixels of each stent film and the uniformly irradiated film without the stent under the same stent holder and settings. Film measurements and Monaco® 5.11 MC calculations show that the dose calculation by TPS using a CT-to-electron density (ED) table with the limit of CT number of 4000 and relative electron density of 2.289, could

Table 2 Dose perturbation ranges of four MBSs measured from 10×5 mm^2 subsets without radiopaque markers at the proximal, distal, left, and right sides using single AP, 4FB, and single arc VMAT techniques

	Proximal (%)	Distal (%)	Left (%)	Right (%)
Single AP technique				
Silicone covered				
Min	−3.1 ± 0.2	−6.4 ± 0.6	−2.3 ± 0.1	−3.8 ± 0.2
Mean	4.2 ± 0.4	−0.6 ± 0.3	5.1 ± 0.3	2.7 ± 0.3
Max	11.5 ± 0.6	6.1 ± 0.1	11.5 ± 0.8	9.1 ± 0.3
Single bare				
Min	−2.4 ± 0.7	−8.4 ± 0.2	−1.4 ± 0.3	−5.0 ± 0.7
Mean	4.7 ± 0.4	−1.9 ± 0.2	4.9 ± 0.4	1.4 ± 0.7
Max	12.8 ± 0.4	4.1 ± 0.5	11.5 ± 0.7	7.6 ± 1.7
Double bare				
Min	0.2 ± 0.7	−10.7 ± 1.4	−1.4 ± 0.1	−3.4 ± 0.1
Mean	7.8 ± 0.2	−3.7 ± 0.5	6.1 ± 0.1	3.8 ± 0.2
Max	15.6 ± 0.4	3.0 ± 0.2	13.2 ± 0.0	10.8 ± 1.3
Large open cell				
Min	−2.7 ± 1.3	−8.6 ± 0.9	−2.0 ± 0.1	−2.6 ± 0.1
Mean	3.8 ± 1.0	−2.0 ± 0.6	4.8 ± 0.0	3.5 ± 0.4
Max	11.2 ± 1.3	4.6 ± 0.7	11.3 ± 0.4	9.8 ± 0.9
4FB technique				
Silicone covered				
Min	−5.5 ± 1.1	−5.0 ± 1.4	−4.1 ± 1.0	−3.5 ± 0.8
Mean	0.4 ± 1.0	0.4 ± 1.7	0.8 ± 1.8	1.9 ± 1.2
Max	6.1 ± 1.1	5.2 ± 1.5	6.7 ± 1.4	6.9 ± 2.4
Single bare				
Min	−3.9 ± 0.6	−4.6 ± 1.2	−2.6 ± 0.1	−3.6 ± 1.1
Mean	1.7 ± 1.2	0.8 ± 1.5	2.2 ± 1.1	2.7 ± 1.5
Max	7.0 ± 2.0	6.2 ± 1.2	8.4 ± 0.5	7.9 ± 2.1
Double bare				
Min	−3.3 ± 0.4	−6.2 ± 0.2	−2.6 ± 0.9	−4.0 ± 0.9
Mean	2.4 ± 0.6	−0.2 ± 1.0	3.5 ± 0.9	2.1 ± 1.2
Max	8.6 ± 1.1	5.3 ± 1.8	9.2 ± 0.5	7.9 ± 1.8
Large open cell				
Min	−6.5 ± 0.2	−5.5 ± 0.2	−5.2 ± 0.3	−4.1 ± 0.1
Mean	−0.2 ± 0.3	0.1 ± 0.8	0.2 ± 0.6	1.3 ± 0.5
Max	7.4 ± 0.2	6.3 ± 1.5	7.1 ± 0.8	7.3 ± 1.3
Single arc VMAT				
Silicone covered				
Min	−4.5 ± 1.3	−6.5 ± 0.9	−7.3 ± 0.8	−4.5 ± 0.9
Mean	2.1 ± 1.2	−0.5 ± 1.2	−1.4 ± 1.1	1.6 ± 1.3
Max	7.9 ± 2.1	6.3 ± 1.3	5.1 ± 1.1	8.0 ± 1.7
Single bare				
Min	−2.0 ± 0.3	−5.7 ± 1.5	−4.8 ± 0.8	−3.1 ± 1.0
Mean	3.2 ± 0.8	0.4 ± 1.3	1.2 ± 1.2	1.8 ± 1.0
Max	9.0 ± 2.3	6.8 ± 2.0	6.6 ± 1.8	7.0 ± 1.9
Double bare				
Min	0.1 ± 0.1	−5.7 ± 0.7	−5.5 ± 0.2	−2.4 ± 0.7
Mean	6.2 ± 0.7	0.8 ± 0.7	0.7 ± 0.8	3.1 ± 0.8
Max	12.8 ± 1.7	7.4 ± 1.2	6.5 ± 1.8	8.9 ± 1.5
Large open cell				
Min	−3.9 ± 0.1	−5.8 ± 0.8	−6.0 ± 0.8	−3.7 ± 1.8
Mean	2.3 ± 0.4	0.3 ± 0.8	−0.4 ± 1.4	1.7 ± 1.2
Max	9.8 ± 0.3	8.4 ± 1.3	5.4 ± 0.1	7.7 ± 0.7

Percent difference (%) = (measured at each stent − measured at no stent)/measured at no stent × 100%. The uncertainty estimate associated with a measurement result was based on the average absolute deviation of the two measurements

differ near the radiopaque markers, leading to approximately 10% considering that the uncertainty of up to 2.2% occurred at the interface of the air cavity. The maximum value in the CT-to-ED table could be altered through the construction of a new calibration curve that contains high values in the CT scanner/TPS set. However, the CT number could be only extended to 5000 and the relative ED of radiopaque markers was not provided by the supplier.

Previously, Mayo-Smith et al. [24] examined the attenuation effects of biliary stents and reported no detectable dose perturbation at 5 cm away from a stent. They used old-fashioned biliary stents including the prototype metallic stent, which may be different from the design and compositions of the current MBSs because modifications of the stent or a new design were constantly introduced for the decades. In addition, their measurements were based on high-dose-rate brachytherapy and locations not at the interface between the stent and surrounding tissues. To date, the dosimetric effect of MBSs during external beam radiotherapy has not been reported. To our knowledge, this study seems the first to quantify the dosimetry differences of clinically available MBSs in a phantom. Although our intent is not to recommend a particular stent, as all clinically available MBSs have the radiopaque markers that produce the biggest dose change, the double bare stent demonstrated the highest dose enhancement, and the large open cell stent had a less prominent effect.

There are practical considerations for further investigations. (1) Since the small diameter of MBSs considered in our study made it impossible to wrap the film around the stent, small pieces of film were placed at the proximal, distal, left, and right sides. Although the selection of small ROIs with 54×5 mm^2 subsets could increase dosimetric uncertainties if there is a positional error, the computer-aided design of the 3D-printed stent holder could allow for more precise measurement setup to achieve positional reproducibility. (2) The precision of the 3D printing system is determined by the printing layer thickness and nozzle diameter. Considering the printing time, the printing layer thickness and nozzle size were set to 2.5 mm and

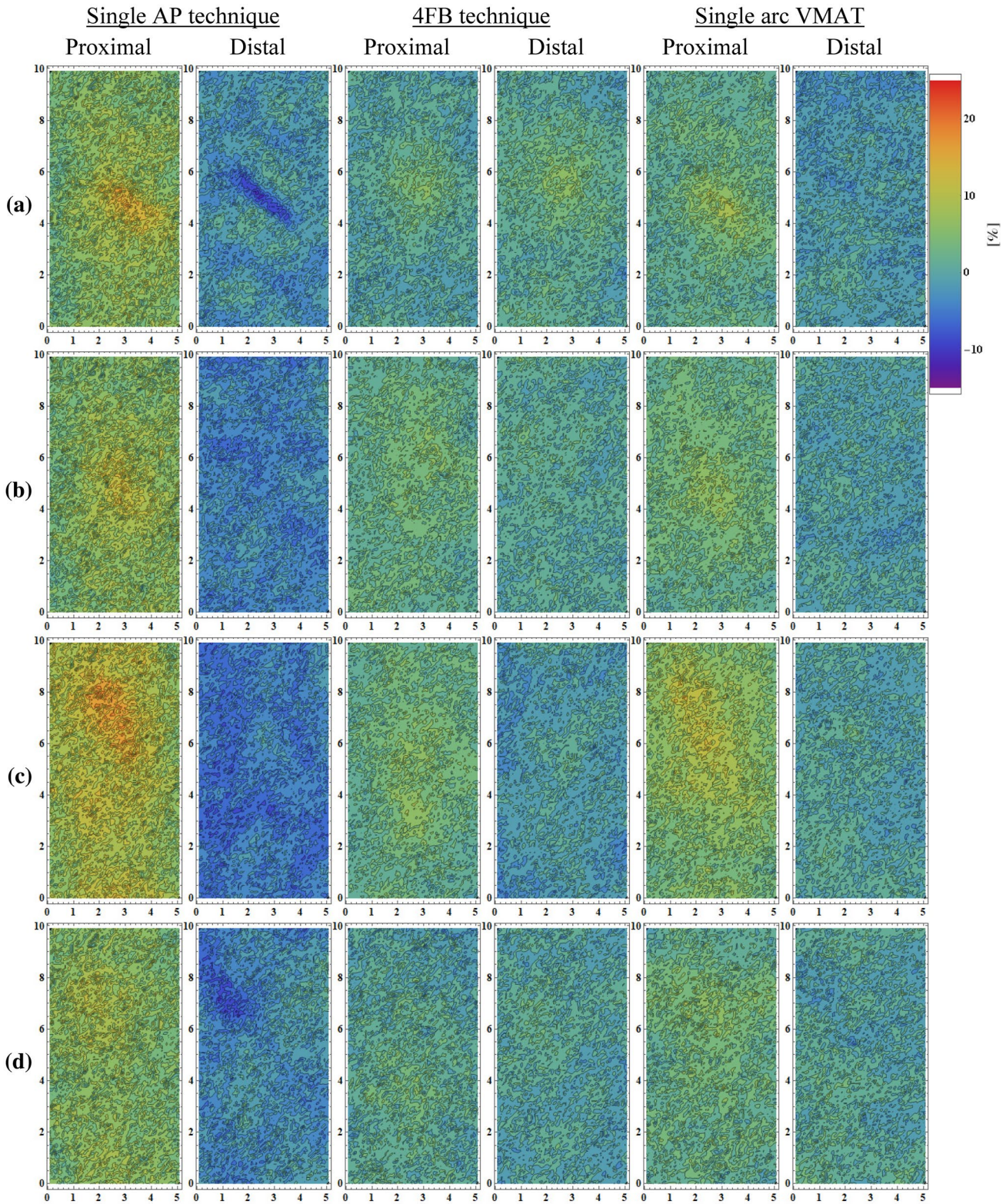

Fig. 5 Visual comparisons of the patterns of dose perturbations on 10×5 mm^2 subsets including a radiopaque marker at the center of each film: **a** silicone covered stent, **b** single bare stent, **c** double bare stent, and **d** large open cell stent measured at the proximal (first column) and distal (second column) sides in AP beam delivery, at the proximal (third column) and distal (fourth column) sides in 4FB beam delivery, and at the proximal (fifth column) and distal (sixth column) sides in single arc VMAT delivery

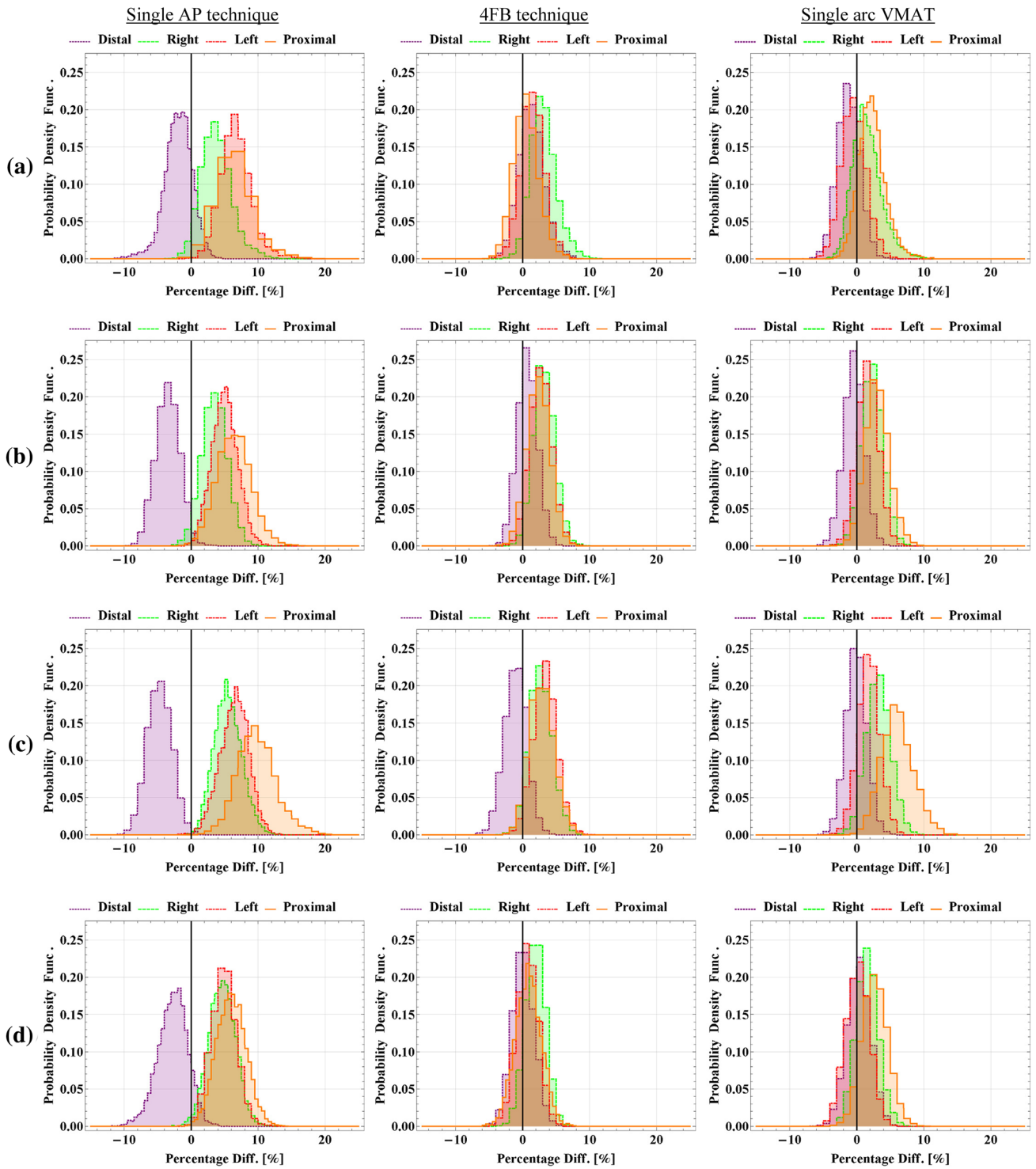

Fig. 6 A degree of overlap between dose histograms to quantify dose perturbations on 10×5 mm^2 subsets including a radiopaque marker at the center of each film measured at four locations next to each MBS using AP, 4FB, and VMAT techniques: **a** silicone covered stent, **b** single bare stent, **c** double bare stent, and **d** large open cell stent

0.5 mm, respectively, in the present study. If these parameters are set to a smaller value, the manufacturing precision will be increased. (3) Although a PLA filament to create the custom stent holder was used to mimic the tissue environment, Acrylonitrile-Butadiene Styrene (ABS) can be preferentially considered as a tissue-equivalent

Table 3 Comparisons of percent differences between the measured and calculated doses at locations proximal and distal to the radiation source using single AP, 4FB, and single arc VMAT techniques with four MBSs, according to the following formula: (calculated − measured)/measured × 100%

	Percent differences (%)					
	Proximal			Distal		
	Minimum	Mean	Maximum	Minimum	Mean	Maximum
Single AP technique						
No stent		0.8			−0.5	
Silicone covered	−3.4	−2.3	−9.0	5.9	3.1	−1.0
Single bare	0.6	−2.1	−8.7	9.6	5.3	−0.4
Double bare	−5.5	−7.1	−12.8	5.8	3.7	−4.0
Large open cell	−3.3	−2.4	−7.6	3.8	3.6	−2.2
4FB technique						
No stent		0.8			0.4	
Silicone covered	2.1	−2.5	1.8	2.3	1.6	−2.9
Single bare	5.2	1.0	−3.3	6.0	1.6	−1.8
Double bare	1.4	−0.9	−5.3	4.7	1.6	−5.0
Large open cell	0.1	1.5	−3.0	4.6	1.9	−2.9
Single arc VMAT						
No stent		2.1			2.2	
Silicone covered	4.5	1.5	−3.2	10.0	5.8	1.9
Single bare	2.5	−0.2	−2.2	1.1	3.2	−0.4
Double bare	−2.9	−3.5	−5.7	−0.2	1.8	−1.4
Large open cell	3.8	0.4	−0.5	1.0	2.7	−2.0

material. The difference between densities of PLA and ABS is of minor importance because the same custom stent holder was used for every MBS. (4) Measurement error causes uncertainty about the value of the measured quantity. Although the measurement error can be estimated by statistical methods, in our study, there were two repeated measurements available for estimating the errors in the measurements. The average absolute deviation was thus used to express the variation between the two measurements. This statistic tells us the difference between the mean value and the individual value. If more measurements are available for examination, this estimate of the difference will be improved.

In conclusion, radiation dose perturbations were observed in clinically available MBS. The main dose escalation was caused by the radiopaque components in the stent. The use of multiple beams including parallel-opposed pairs reduced dose perturbations caused by the nitinol and radiopaque markers within the stent. In clinical routine a MBS is never implanted in an ideal way. Modern 3D-planning procedures are based on several beam directions, segmented beams and beam weightings. Further problem is that in most TPS systems small structures like radiopaque markers or the mesh of the stent are not recognized. Up to now the dosimetrist needs to keep dose perturbations around the MBS in mind in order to give a hint to the radio-oncologist. Special attention is thus required for patients in whom the radiopaque markers are closely located near critical structures or the target volume, which could allow safer use of MBS by mitigating the potential risk of either overdose or underdose.

Funding This research was supported by a Grant of the Radiation Technology R&D program through the National Research Foundation of Korea funded by the Ministry of Science, ICT & Future Planning (2017M2A2A6A01070330).

Compliance with ethical standards

Conflict of interest The authors declare that they have no conflict of interest.

Ethical approval This article does not contain any studies with human participants or animals performed by any of the authors.

References

1. Oettle H, Neuhaus P, Hochhaus A, Hartmann JT, Gellert K, Ridwelski K, Niedergethmann M, Zülke C, Fahlke J, Arning MB (2013) Adjuvant chemotherapy with gemcitabine and long-term outcomes among patients with resected pancreatic cancer: the CONKO-001 randomized trial. JAMA 310(14):1473–1481
2. Li D, Xie K, Wolff R, Abbruzzese JL (2004) Pancreatic cancer. Lancet 363(9414):1049–1057
3. Beltrán MB, Allal AS, Gich I, Solé JM, Carrió I (2012) Is adjuvant radiotherapy needed after curative resection of extrahepatic biliary tract cancers? A systematic review with a meta-analysis of observational studies. Cancer Treat Rev 38(2):111–119

4. Hsu CC, Herman JM, Corsini MM, Winter JM, Callister MD, Haddock MG, Cameron JL, Pawlik TM, Schulick RD, Wolfgang CL (2010) Adjuvant chemoradiation for pancreatic adenocarcinoma: the Johns Hopkins Hospital—Mayo Clinic collaborative study. Ann Surg Oncol 17(4):981–990
5. Glinka J, Diaz F, Alva A, Mazza O, Claria RS, Ardiles V, de Santibañes E, Pekolj J, de Santibañes M, Roj J (2018) Use of radiotherapy in patients with palliative double bypass for locally advanced pancreatic adenocarcinoma. Radiat Oncol J 36(3):210–217
6. Atwood TF, Hsu A, Ogara MM, Luba DG, Tamler BJ, DiSario JA, Maxim PG (2012) Radiotherapy dose perturbation of esophageal stents examined in an experimental model. Int J Radiat Oncol Biol Phys 82(5):1659–1664
7. Chen YK, Schefter TE, Newman F (2011) Esophageal cancer patients undergoing external beam radiation after placement of self-expandable metal stents: is there a risk of radiation dose enhancement? Gastrointest Endosc 73(6):1109–1114
8. Li XA, Chibani O, Greenwald B, Suntharalingam M (2002) Radiotherapy dose perturbation of metallic esophageal stents. Int J Radiat Oncol Biol Phys 54(4):1276–1285
9. Dayyeh BA, Vandamme J, Miller RC, Baron TH (2013) Esophageal self-expandable stent material and mesh grid density are the major determining factors of external beam radiation dose perturbation: results from a phantom model. Endoscopy 45(1):42–47
10. Francis SR, Anker CJ, Wang B, Williams GV, Cox K, Adler DG, Shrieve DC, Salter BJ (2013) Self-expanding stent effects on radiation dosimetry in esophageal cancer. J Appl Clin Med Phys 14(4):121–135
11. Tsuji Y, Yoshimura H, Uto F, Tamada T, Iwata K, Tamamoto T, Asakawa I, Shinkai T, Kichikawa K, Hasegawa M (2007) Physical and histopathological assessment of the effects of metallic stents on radiation therapy. J Radiat Res 48(6):477–483
12. Elhammali A, Patel M, Weinberg B, Verma V, Liu J, Olsen JR, Gay HA (2015) Late gastrointestinal tissue effects after hypofractionated radiation therapy of the pancreas. Radiat Oncol 10(1):1–8
13. Marks LB, Yorke ED, Jackson A, Ten Haken RK, Constine LS, Eisbruch A, Bentzen SM, Nam J, Deasy JO (2010) Use of normal tissue complication probability models in the clinic. Int J Radiat Oncol Biol Phys 76(3):S10–S19
14. Cho B (2018) Intensity-modulated radiation therapy: a review with a physics perspective. Radiat Oncol J 36(1):1
15. Pfau PR, Pleskow DK, Banerjee S, Barth BA, Bhat YM, Desilets DJ, Gottlieb KT, Maple JT, Siddiqui UD, Tokar JL (2013) Pancreatic and biliary stents. Gastrointest Endosc 77(3):319–327
16. Dumonceau J-M, Heresbach D, Devière J, Costamagna G, Beilenhoff U, Riphaus A (2011) Biliary stents: models and methods for endoscopic stenting. Endoscopy 43(07):617–626
17. Kim M-J, Lee S-R, Lee M-Y, Sohn JW, Yun HG, Choi JY, Jeon SW, Suh TS (2017) Characterization of 3D printing techniques: toward patient specific quality assurance spine-shaped phantom for stereotactic body radiation therapy. PLoS ONE 12(5):e0176227
18. Kamomae T, Shimizu H, Nakaya T, Okudaira K, Aoyama T, Oguchi H, Komori M, Kawamura M, Ohtakara K, Monzen H (2017) Three-dimensional printer-generated patient-specific phantom for artificial in vivo dosimetry in radiotherapy quality assurance. Phys Med 44:205–211
19. Yoon J, Park K, Kim JS, Kim YB, Lee H (2019) Skin dose comparison of cyberknife and helical tomotherapy for head-and-neck stereotactic body radiotherapy. Prog Med Phys 30(1):1–6
20. Park J, Yea JW (2019) Whole brain radiotherapy using four-field box technique with tilting baseplate for parotid gland sparing. Radiat Oncol J 37(1):22–29
21. Niroomand-Rad A, Blackwell CR, Coursey BM, Gall KP, Galvin JM, McLaughlin WL, Meigooni AS, Nath R, Rodgers JE, Soares CG (1998) Radiochromic film dosimetry: recommendations of AAPM radiation therapy committee task group 55. Med Phys 25(11):2093–2115
22. Dreindl R, Georg D, Stock M (2014) Radiochromic film dosimetry: considerations on precision and accuracy for EBT2 and EBT3 type films. Z Med Phy 24(2):153–163
23. ICRU Report 83 (2010) Prescribing, recording, and reporting photon-beam intensity-modulated radiation therapy (IMRT) 10. Oxford University Press, Oxford
24. Mayo-Smith WW, Dawson SL, Mauceri T, Mueller PR (1996) Attenuation effects of biliary endoprostheses on therapeutic radiation. Radiology 199(2):571–572